DOI: 10.13009/EUCASS2025-722
11TH EUROPEAN CONFERENCE FOR AERONAUTICS AND SPACE SCIENCES (EUCASS)

Rapid Stagnation Heat Flux Prediction on Parametric Nose Cones in Hypersonic Flow via Variational Autoencoding

Oguz Kaan Sevinc[⋆†] *and Huseyin Avni Yasar*[⋆]
[⋆]*Roketsan Inc.*
06852 Ankara Turkiye
oguzksevinc@gmail.com · yasarr.avni@gmail.com
[†]Corresponding author

Abstract

Reliable prediction of stagnation point heat flux is essential for hypersonic vehicle design, yet high-fidelity simulations remain computationally demanding, limiting rapid design evaluations. This study introduces a surrogate approach utilizing a variational autoencoder (VAE) to encode nose cone geometries into a compact latent space, combined with a conditional multi-layer perceptron (MLP) to estimate stagnation point heat flux. The method accurately predicts heat flux with a significantly reduced subset of the entire design space, greatly reducing computational effort. Additionally, the model maintains accuracy for predictions beyond the original training conditions, offering a practical and efficient alternative to traditional CFD methods.

1. Introduction

Hypersonic vehicles operate in environments characterized by intense shockwaves, high temperature gas chemistry, and substantial heat fluxes. These extreme conditions require a well designed thermal protection system. As a result, accurately predicting reentry conditions and designing thermal protection systems properly are essential for any vehicle undergoing atmospheric entry.

The stagnation point heat flux is one of the most critical parameters in the design of a hypersonic reentry vehicle, as it represents the maximum heat load experienced during flight. This value plays a crucial role in the vehicle's thermal management and the structural integrity of its thermal protection system. Therefore, accurately determining the stagnation point heat flux is essential.[1,2]

Since the magnitude of stagnation point heat flux is highly influenced by the vehicle's geometry, the design of the nose cone becomes a key factor in shaping the thermal and aerodynamic environment. During high speed atmospheric flight or reentry, the intense compression of air leads to severe heating, especially around the nose region. Evaluating different nose cone geometries is therefore essential to understand how shape influences the heat flux encountered in these extreme conditions.[3]

Although computational fluid dynamics (CFD) offers high-fidelity predictions of heat flux for various nose cone geometries, its computational cost grows significantly with increasing geometric and flow field complexity. Even with improvements in computing capabilities, CFD simulations of complex hypersonic flows remain resource intensive. This challenge has led to the search for alternative methods that can deliver comparable accuracy with greater computational efficiency.

Classical surrogate models such as Kriging, radial basis functions, and artificial neural networks have been widely employed in hypersonic heating studies.[4–6] However, they often assume parameterized geometries and require dense datasets to maintain prediction accuracy. More recent efforts have explored physics-informed neural networks (PINNs)[7–9] and multi-fidelity frameworks that blend low and high-fidelity simulations,[10,11] with advanced neural architectures further improving data efficiency in sparse regimes.[12] These approaches reduce dependency on large high-fidelity datasets by either embedding governing equations directly into the training loss or learning hierarchical mappings across fidelity levels. In our previous work, a PINN-based formulation was also applied to estimate stagnation-point heat flux on axisymmetric blunt bodies, demonstrating improved accuracy under data-scarce conditions.[13]

Despite these advancements, a critical limitation persists: existing models primarily rely on explicitly defined geometry parameters. For shape families like nose cones, where different analytic profiles involve distinct equations,

DOI: 10.13009/EUCASS2025-722

mapping them to a unified set of inputs becomes impractical. Consequently, directly using geometric images rather than analytical parameters becomes a more generalizable solution.

Recent studies have begun to explore geometry-aware surrogates using variational autoencoders (VAEs) to compress shapes into latent representations,[14–16] which are then fused with flow conditions for inference. These methods have shown promise in airfoil and wing design problems. However, such latent models remain underexplored for hypersonic applications, particularly in predicting critical quantities, such as stagnation point heat flux, across diverse nose cone families.

In this study, a predictive framework is developed by combining a variational autoencoder (VAE) for compact geometric encoding with a conditional multi-layer perceptron (MLP) that estimates stagnation point heat flux in hypersonic flow conditions. The models are trained on carefully sampled subsets of the full design space, covering a wide range of geometric profiles and flight conditions. By integrating effective shape encoding with targeted training strategies and hyperparameter tuning, the proposed approach offers accurate heat flux predictions across both seen and unseen configurations, enabling efficient exploration of geometry–flight condition combinations with reduced simulation cost.

2. Methodology

2.1 Problem Definition

In this study, CFD analyses are performed to calculate the stagnation point heat flux on four different nose cone types under hypersonic flow conditions using the ICFD++ software from Metacomp Technologies. The model is constructed as an axisymmetric body featuring different types of nose cone shapes. An example of the analysis domain is shown in Figure 1, which displays a power series nose cone along with the boundary condition labels used in the CFD simulations. The same setup is applied across all analyses conducted in this work. The wall boundary condition is isothermal wall with a fixed wall temperature of 300 Kelvin. Freestream pressure, temperature, and velocity are specified at the inlet. The outlet is defined as a supersonic outlet. The working fluid is air, and the flow is modeled as compressible, viscous, and laminar.

Table 1: Boundary conditions for mesh independence study

Parameter	**Value**
Geometry	Power series
Mach number	9
Altitude	5 km
Freestream pressure	54050 Pa
Freestream temperature	256 K
Freestream density	0.7328 kg/m^3

A thermally perfect (calorically imperfect) air model is used to accurately capture the gas behavior under the rising temperature levels of hypersonic flow. The calorically perfect gas assumption where specific heats Cp and Cv are treated as constants is only valid over a limited temperature range, which is generally below 450 Kelvin for air. However, at higher temperatures the excitation of vibrational energy modes causes these parameters to increase with temperature. The thermally perfect air model accounts for this by allowing specific heat to vary as a function of temperature while still assuming a fixed chemical composition and ideal gas behavior.[17]

Table 2: Mesh independence study results

Mesh Name	**Cells**	**Stagnation Heat Flux (MW/m^2)**
Mesh 1	20,336	19.8
Mesh 2	40,991	15.6
Mesh 3	48,357	14.1
Mesh 4	62,196	14.0

To ensure reliable results for different nose cone configurations, a mesh independence study is carried out for the generation of computational grids. In this study, the first layer thickness of the boundary layer is kept constant for all

DOI: 10.13009/EUCASS2025-722

mesh cases to maintain a wall cell Reynolds number below 1. In the context of CFD meshing, the wall cell Reynolds number Re_{cw} can be defined as:

$$Re_{cw} = \frac{\rho_w a_w \Delta y}{\mu_w} \tag{1}$$

where ρ_w is the density of flow at the wall, a_w is the sound speed at the wall, μ_w is the viscosity of flow at the wall, and Δy is the first layer thickness.[18]

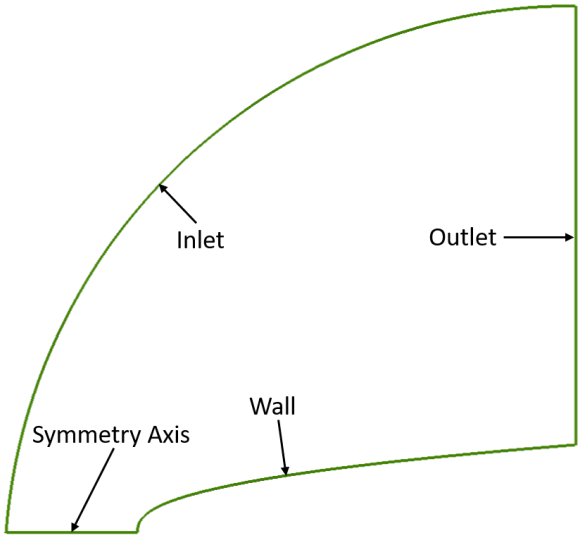

Figure 1: Boundary conditions used for the analysis

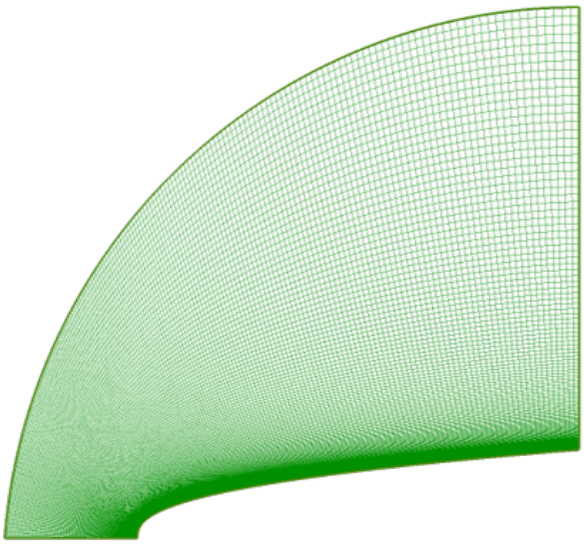

Figure 2: Sample mesh structure

The mesh independence study focuses on the number of layers, the growth rate, and the point spacing along the nose wall near the stagnation region. The study is conducted using a randomly selected geometry from a set of 320 different nose cone configurations. The flow condition is chosen as the most challenging case corresponding to the highest expected heat flux within the scope of this work. Computations are performed using the boundary conditions listed in Table 1. The results of the mesh study are presented in Table 2. Based on these results, Mesh 3 shown in Figure 2 is selected since the difference between Mesh 3 and Mesh 4 is less than 1%. An example case showing the Mach number and temperature distributions obtained by using the boundary conditions in Table 2 and Mesh 3 is shown in Figure 3.

DOI: 10.13009/EUCASS2025-722

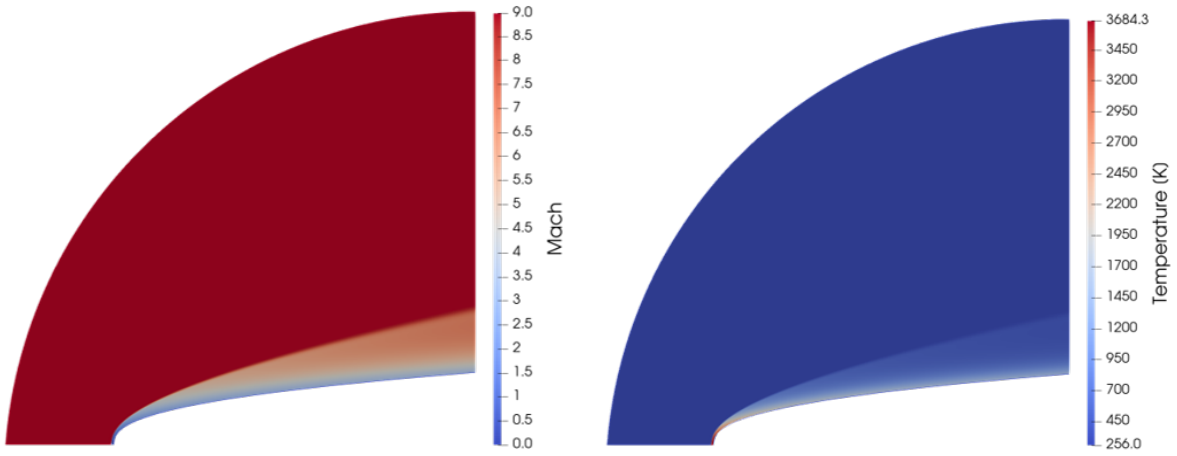

(a) Mach (b) Temperature

Figure 3: Resultant Mach number and temperature distribution

2.2 Parametric Formulations of Nose Cone Profiles

In hypersonic flight, the nose cone is one of the main focus points of aerodynamic heating due to its direct interaction with the bow shock. A blunt nose causes the bow shock to detach and stand off from the surface, reducing the stagnation point heat flux compared to sharp geometries, which generate attached shocks and higher localized heating. This is an important part of hypersonic vehicle design, where nose geometry is carefully chosen to balance different requirements.[19]

Building on this balance between thermal protection and aerodynamic performance, the selection of nose cone geometry for hypersonic vehicles must consider both mission objectives and design constraints. The Haack series offers the lowest wave drag at Mach 5+ conditions, but its sharp tip leads to high stagnation point heating. Moderately blunted profiles such as parabolic or secant ogive shapes with small spherical caps can reduce peak heat flux with minimal drag increase with specific fineness ratios.[20,21]

The parametric nose cone profiles used in this study are defined by the following equations, where $x \in [0, L]$ is the axial coordinate, L is the length of the nose cone and R is the base radius. In addition, each formulation uses a shape parameter specific to the family.[22]

Power series nose cones are defined by a shape that becomes sharper as the exponent n approaches 1 (a cone) and blunter as n approaches 0 (a flat cylinder). It typically features a blunt tip and a non-tangent base, though the base is often modified to smooth out the slope discontinuity and improve flow attachment. The equation used to create the power series can be defined as:

$$y(x) = R\left(\frac{x}{L}\right)^n \tag{2}$$

Secant ogive nose cones are formed from a segment of a circle where the base does not lie on the circle's radius. This results in a sharper profile and a non-tangent intersection with the body that introduces a slight geometric discontinuity. The equations used to create the secant ogive can be defined as:

$$\rho > \frac{R^2 + L^2}{2R} \tag{3}$$

$$\alpha = \tan^{-1}\left(\frac{R}{L}\right) - \cos^{-1}\left(\frac{L^2 + R^2}{4\rho^2}\right)^{1/2} \tag{4}$$

$$y(x) = \left[\rho^2 - (x - \rho\cos\alpha)^2\right]^{1/2} + \rho\sin\alpha \tag{5}$$

Parabolic series nose cones are formed by rotating a segment of a parabola, producing a sharp tipped, smoothly curving profile that is tangent to the body when a full parabola segment is used. The equation used to create the secant ogive by using the shape coefficient K can be defined as:

DOI: 10.13009/EUCASS2025-722

$$y(x) = R \cdot \frac{2(x/L) - K(x/L)^2}{2 - K} \tag{6}$$

Haack series nose cones are mathematically derived to minimize wave drag, with the Von Kármán profile being the most widely used variant due to its aerodynamic efficiency. These shapes have a smooth, gradually increasing curvature that is nearly tangent to the body, and their tips are slightly rounded rather than perfectly sharp. The equations used to create the Haack series by using the shape factor C can be defined as:

$$\theta(x) = \cos^{-1}\left(1 - \frac{2x}{L}\right) \tag{7}$$

$$y(x) = R \cdot \left[\frac{1}{\pi}\left(\theta - \frac{1}{2}\sin(2\theta) + C\sin^3\theta\right)\right]^{1/2} \tag{8}$$

2.3 Dataset

The initial stage of this study involves generating a comprehensive design database comprising 320 unique nose cone geometries, as shown in Figure 4. These shapes are procedurally defined using parametric equations from four different nose cone series: power, secant ogive, parabolic, and Haack. Each profile is sampled across its respective shape parameter range and a common global radius, as listed in Table 3. For consistency, the nose cone length L is normalized to unity across all profiles.

Table 3: Geometric parameter ranges used in generating 320 nose cone profiles

Parameter Type	Profile Type	Parameter	Range
Profile-specific	Power series	Shape factor n	0.40 – 0.80
	Secant ogive	ρ/R ratio	1.43 – 4.75
	Parabolic	Shape coefficient K	0.50 – 1.10
	Haack series	Shape factor C	0.00 – 1.00
Global	All Profiles	Radius R	0.20 – 0.65

Each of these 320 geometries is evaluated under five Mach numbers and five altitudes, forming a total of 25 freestream conditions per geometry and yielding a complete design space of $320 \times 25 = 8000$ unique cases. Table 4 summarizes the range of physical conditions.

Table 4: Freestream condition variables

Variable	Description	Values
Ma	Mach number	5, 6, 7, 8, 9
h	Altitude (km)	5, 10, 15, 20, 25

The geometries are visualized as 128×128 binary images representing filled shape masks, as shown in Figure 4. These pixel-based contours are not suitable for direct input into regression models. To integrate them into neural networks, they must be encoded into low-dimensional vectors, a task later addressed via a variational autoencoder.

To ensure broad coverage of the design space while minimizing computational cost, subsets of varying sizes with 2000, 2500, 3000, and 3500 points are selected from the full set of 8000 cases. Sampling is performed using Latin Hypercube Sampling (LHS),[23] a stratified technique known to produce more representative and space-filling sample distributions than purely random methods. Each subset aims to maintain geometric and physical diversity across the input space, enabling effective training of surrogate models.

Once the samples are selected, a consistent preprocessing pipeline is applied. The output variable, critical heat flux, exhibits a highly skewed distribution across several orders of magnitude, ranging approximately from 10^4 to 10^9. To mitigate this imbalance and improve numerical stability during training, a logarithmic transformation is applied to the output. Following this, all features and transformed outputs are normalized to the range $[0, 1]$ using min–max scaling:

$$\mathbb{X}^{sc} = \frac{\mathbb{X}^{raw} - \mathbb{X}^{raw}_{\min}}{\mathbb{X}^{raw}_{\max} - \mathbb{X}^{raw}_{\min}}, \tag{9}$$

DOI: 10.13009/EUCASS2025-722

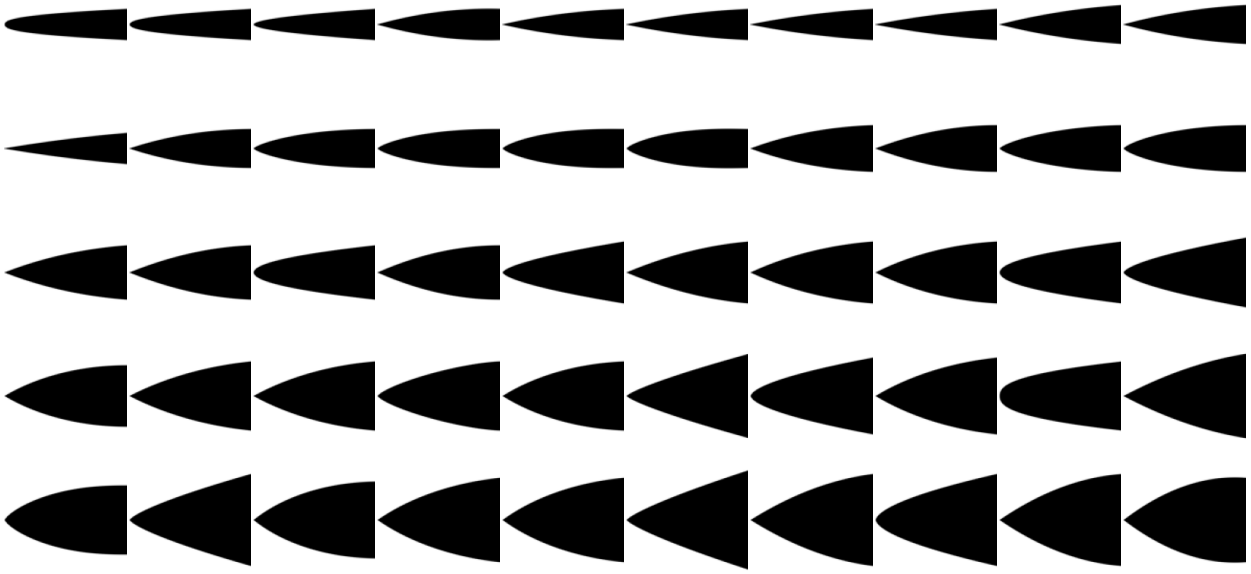

Figure 4: Representative samples of the generated nose cone geometry database.

where $\mathbb{X}^{sc}$ and $\mathbb{X}^{raw}$ refer to the scaled and raw data vectors respectively, and $\mathbb{X}^{raw}_{\min}$, $\mathbb{X}^{raw}_{\max}$ denote the minimum and maximum values computed feature-wise across the dataset.

To reduce potential distributional shifts between training and evaluation splits, the data is partitioned using the data twinning algorithm proposed in.[24] This method ensures that the validation set closely reflects the distribution of the training set while maintaining disjoint membership. The remaining data, not selected for training or validation, serves as an out-of-domain holdout set for evaluating extrapolation performance.

2.4 Feature Extraction Based on VAE

2.4.1 Architecture

As described in the previous section, a dataset of nose cone geometries is constructed using parametric shape functions across several cone profiles. While these representations define valid physical contours, they exist only as pixel-level masks and cannot be directly utilized in optimization or surrogate modeling pipelines. To enable efficient learning and design exploration, it is essential to extract compact and informative representations that capture the geometric variability among designs.

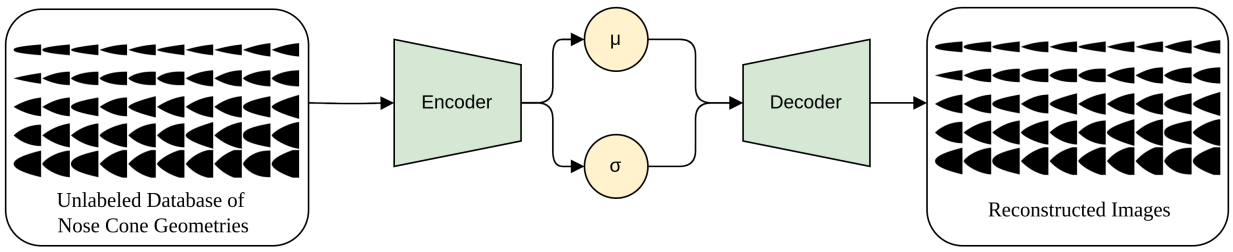

Figure 5: VAE pipeline for nose cone geometry encoding.

To this end, a convolutional variational autoencoder (VAE) is employed for unsupervised feature extraction. Each nose cone shape is rasterized into a 128×128×1 binary image representing its silhouette. Prior to training, images are normalized to lie within $[-1, 1]$, centered within the canvas, and proportionally scaled to maintain consistent spatial framing.

The encoder consists of three convolutional layers with batch normalization and LeakyReLU activations, followed by two parallel fully connected layers that predict the latent distribution parameters μ and $\log \sigma^2$. The decoder

DOI: 10.13009/EUCASS2025-722

Table 5: VAE architecture used for image encoding (input: $128 \times 128 \times 1$, latent dimension: 32)

Stage	Layer	Output dim.	Kernel / stride / pad	Activation
Encoder				
Input	–	$128 \times 128 \times 1$	–	–
Conv 1	Conv2D+BN	$64 \times 64 \times 16$	3/2/1	LeakyReLU(0.2)
Conv 2	Conv2D+BN	$32 \times 32 \times 32$	3/2/1	LeakyReLU(0.2)
Conv 3	Conv2D+BN	$16 \times 16 \times 64$	3/2/1	LeakyReLU(0.2)
Flatten	–	32768	–	–
FC μ	Linear	32	–	(linear)
FC $\log \sigma^2$	Linear	32	–	(linear)
Decoder				
Latent	Input z	32	–	–
FC	Linear	32768	–	LeakyReLU(0.2)
Reshape	–	$16 \times 16 \times 64$	–	–
DeConv 1	ConvT+BN	$32 \times 32 \times 32$	3/2/1	LeakyReLU(0.2)
DeConv 2	ConvT+BN	$64 \times 64 \times 16$	3/2/1	LeakyReLU(0.2)
DeConv 3	ConvT	$128 \times 128 \times 1$	3/2/1	Tanh

reconstructs input geometries using a transposed convolutional stack and a final `tanh` activation to ensure output compatibility with the normalized input range. Batch Normalization helps stabilize learning, while LeakyReLU with a small negative slope (0.2) mitigates vanishing gradients. Sampling is performed via the reparameterization trick. The full architecture is illustrated in Figure 5, with detailed layer specifications listed in Table 5.

2.4.2 Performance Metrics

The training objective of a VAE minimizes the negative evidence lower bound (ELBO):

$$\mathcal{L}_{\text{VAE}} = -\frac{1}{N}\sum_{i=1}^{N} \log p_\theta(\mathbf{x}_i \mid \mathbf{z}_i) \; + \; \frac{1}{2}\sum_{j=1}^{d}\left(1 + \log \sigma_j^2 - \mu_j^2 - \sigma_j^2\right), \tag{10}$$

where $p_\theta(\mathbf{x}_i \mid \mathbf{z}_i)$ denotes the decoder's likelihood of reconstructing image $\mathbf{x}_i$ from latent $\mathbf{z}_i \sim \mathcal{N}(\mu, \text{diag}(\sigma^2))$.

The first term represents the reconstruction log-likelihood. In this study, it is implemented via mean squared error (MSE) over all image pixels:

$$\mathcal{L}_{\text{rec}} = \frac{1}{N}\sum_{i=1}^{N} \|\mathbf{x}_i - \hat{\mathbf{x}}_i\|_2^2 \tag{11}$$

The second term corresponds to the KL divergence between the latent posterior and a unit Gaussian prior, enforcing regularization of the latent space. Sampling is made differentiable via the reparameterization trick:

$$\mathbf{z} = \mu + \sigma \cdot \varepsilon \quad \text{where} \quad \varepsilon \sim \mathcal{N}(0, I) \tag{12}$$

2.4.3 Training Setup

The model is optimized using Adam with a learning rate of 10^{-3} and L2 weight decay. A KL warm-up strategy gradually increases β from 0 to 0.05 over the first 200 epochs to avoid early posterior collapse. The configuration is summarized in Table 6.

DOI: 10.13009/EUCASS2025-722

Table 6: VAE training hyperparameters

Parameter	Symbol / Setting	Value
Optimizer	Adam	`lr = 1×10`$^{-3}$
KL weight schedule	$\beta(t)$	Linear warmup to 0.05 in 200 epochs
Batch size	B	8
Epochs	$T_{\max}$	500
Weight decay	λ	1×10^{-4}

2.5 Conditional MLP for Heat Flux Prediction

2.5.1 Architecture

The prediction of the stagnation point heat flux from nose cone configurations under various flight conditions is achieved through the training of a deep neural network (DNN) model, utilizing the latent vectors extracted by the encoder of the Variational Autoencoder (VAE). The input to this surrogate regressor consists of a 32-dimensional latent vector $\mathbf{z}$ concatenated with Mach number and altitude values, forming a (34×1) feature vector. The output is a scalar representing the critical heat flux value.

The model architecture is based on a fully connected multi-layer perceptron (MLP) with non-linear activation functions applied after each hidden layer. The forward pass through layer i of the network is defined as:

$$f_i(x, \theta) = \sigma_i(W_i x_i + b_i), \tag{13}$$

where x_i is the input vector to layer i, W_i and b_i denote the learnable weights and biases, and σ_i is the non-linear activation function. The final prediction is computed via function composition:

$$\hat{y}(x) = (f_o \circ f_{o-1} \circ \cdots \circ f_1)(x). \tag{14}$$

The model parameters $\theta = \{W, b\}$ are optimized using backpropagation by minimizing a selected loss metric:

$$\mathcal{L}(x; \theta) = d(y, \hat{y}), \tag{15}$$

where d is the distance function chosen as the training loss. The framework behind the neural network for this problem is shown in Figure 6.

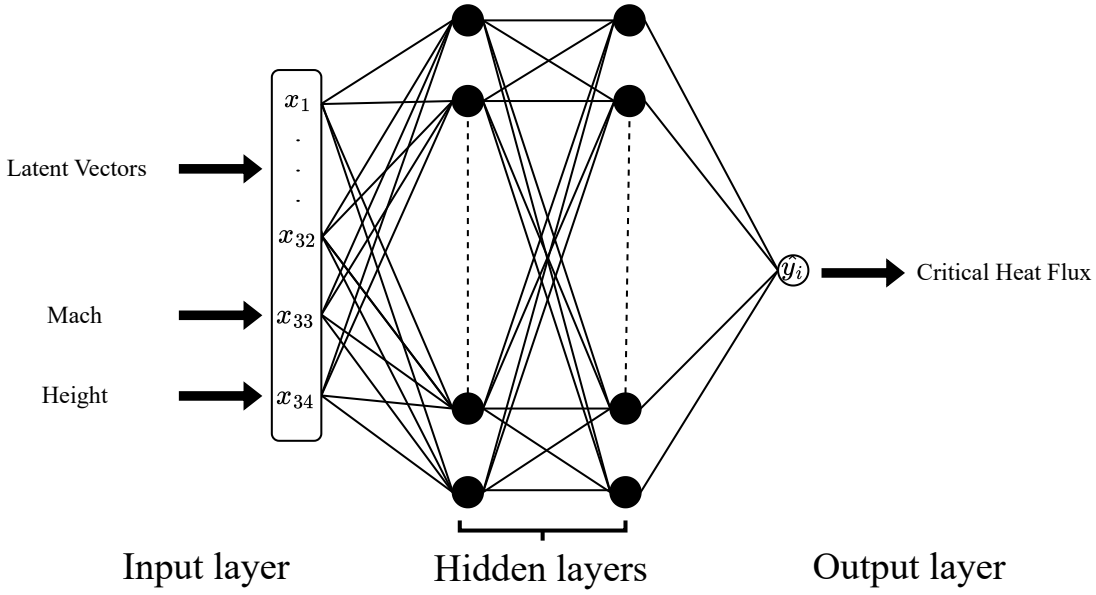

Figure 6: Schematic diagram of surrogate regressor for heat flux prediction based on latent geometry encoding.

DOI: 10.13009/EUCASS2025-722

2.5.2 Performance Metrics

In this study, the accuracy of the model's performance is assessed by comparing the actual (y) and predicted ($\hat{y}$) values for neural network. R-squared (R^2), mean absolute error (MAE), mean absolute percentage error (MAPE), and mean squared error (MSE) values are used as the performance metrics in this work.

The performance of the trained model is evaluated using standard regression metrics, including:

$$R^2 = 1 - \frac{\sum_{i=1}^{N}(y_i - \hat{y}_i)^2}{\sum_{i=1}^{N}(y_i - \overline{y})^2} \tag{16}$$

$$\mathcal{L}_{\text{MAE}} = \frac{1}{N}\sum_{i=1}^{N}|y_i - \hat{y}_i| \tag{17}$$

$$\mathcal{L}_{\text{MSE}} = \frac{1}{N}\sum_{i=1}^{N}(y_i - \hat{y}_i)^2 \tag{18}$$

$$\mathcal{L}_{\text{MAPE}} = \frac{1}{N}\sum_{i=1}^{N}\left|\frac{y_i - \hat{y}_i}{y_i}\right| \tag{19}$$

where y_i and $\hat{y}_i$ are the ground truth and predicted heat flux values and N is the number of training samples.

2.5.3 Hyperparameter Optimization

Hyperparameters control the learning dynamics and representational capacity of neural networks. These include architectural choices such as the number of hidden layers and the number of neurons per layer, as well as optimization-related parameters like learning rate and batch size. A well-defined search space is critical to ensure efficient exploration.

In this study, hyperparameter optimization is conducted using the Optuna framework,[25] which employs a Bayesian optimization strategy with early stopping. The search space is defined as follows: the number of hidden layers is sampled as a discrete integer from 1 to 5, while the number of neurons per layer is sampled as an integer in the range [16, 256]. Learning rate is sampled from a log-uniform distribution over $[1 \times 10^{-4}, 1 \times 10^{-1}]$, and batch size is selected from a discrete set of common powers of two. Table 7 summarizes the parameter ranges considered.

Additionally, a ReduceLROnPlateau scheduler is used to lower the learning rate if the validation loss plateaus for 250 epochs.

Table 7: Hyperparameter search space for MLP

Hyperparameter	**Type**	**Search Range**
Neuron count	Integer	[16, 256]
Number of layers	Integer	[1, 5]
Learning rate	Log-uniform	1×10^{-4} to 1×10^{-1}
Batch size	Categorical	[16, 32, 64, 128, 256]

3. Results & Discussion

3.1 Model Selection and Hyperparameter Tuning Results

As a result of a comprehensive hyperparameter search, the optimum hyperparameters for training datasets ranging from 2000 to 3500 samples are presented in Table 8, which summarizes the optimal configurations selected by Optuna.

Table 8: Optimal hyperparameters for each training–set size

Samples	**Hidden units**	**# Layers**	**Learning rate**	**Batch size**
2000	$240 \to 16 \to 176$	3	2×10^{-3}	32
2500	$208 \to 16 \to 176$	3	2×10^{-3}	16
3000	$208 \to 48 \to 80 \to 144$	4	5×10^{-4}	16
3500	$240 \to 48 \to 144 \to 144$	4	9×10^{-4}	16

DOI: 10.13009/EUCASS2025-722

As expected, larger datasets tend to benefit from deeper architectures with broader layers. For instance, the 3500-point model employs four hidden layers with up to 240 neurons, while the smaller 2000-point model converges effectively with three narrower layers. Across all configurations, relatively low learning rates ($< 10^{-3}$) and smaller batch sizes provided stable convergence and better generalization.

3.2 Performance on Test Set

Table 9 reports the performance metrics on the test sets. As the number of training samples increase, model accuracy improves notably. The MAPE reduces from 3.52% with 2000 samples to just 1.99% with 3500 samples. This consistent drop in error, alongside improvements in MAE, RMSE, and R^2, highlights the model's capacity to extract meaningful representations from the VAE-encoded geometries.

Table 9: Validation set performance across dataset sizes

Design points	MAPE (%)	MAE	RMSE	R^2
2000	3.524	5.276e+05	1.237e+06	0.9950
2500	3.467	4.840e+05	1.249e+06	0.9951
3000	2.470	3.260e+05	9.250e+05	0.9975
3500	1.989	2.735e+05	7.825e+05	0.9983

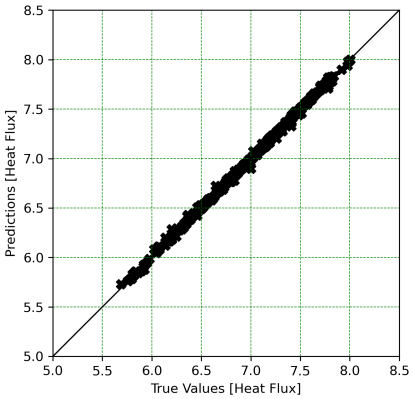

(a) Validation – 2000 Points

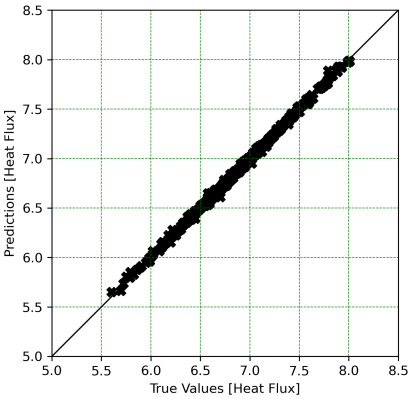

(b) Validation – 2500 Points

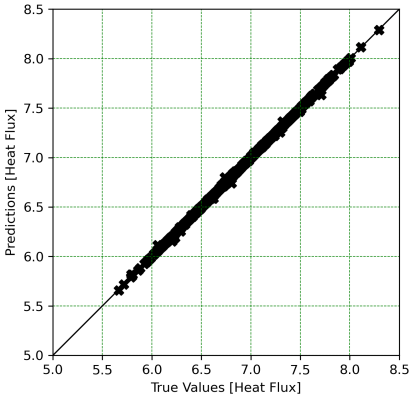

(c) Validation – 3000 Points

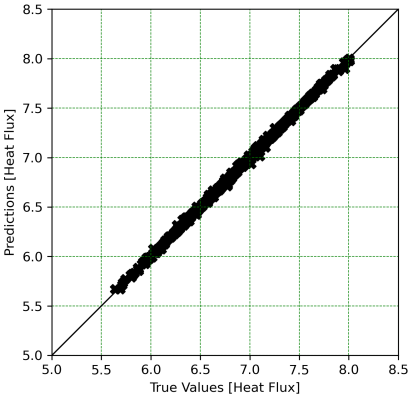

(d) Validation – 3500 Points

Figure 7: Log10 True vs Predicted values for test data across different dataset sizes

Figure 7 shows the predicted versus ground truth heat flux values on a log scale. The alignment around the diagonal line tightens significantly with increasing dataset size. Additionally, Figure 8 illustrates the shift in the error distribution, showing narrower and lower-median MAPE for larger datasets.

DOI: 10.13009/EUCASS2025-722

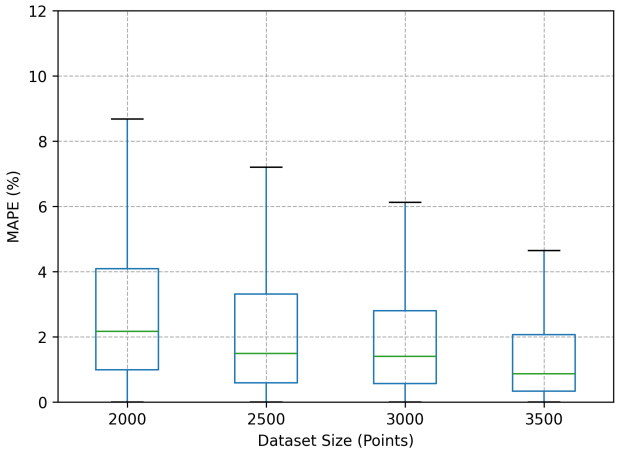

Figure 8: MAPE distribution across test splits

3.3 Performance on Unseen Set in Outside Points

The generalization capability of the models is further assessed by evaluating their performance on a completely unseen dataset drawn from regions of the design space not used during training or validation. As summarized in Table 10, the model still maintains reasonable accuracy, even in extrapolative regimes. The MAPE drops from 4.42% at 2000 points to 2.35% at 3500 points. This smooth reduction in error indicates that the learned latent representations, combined with flight condition inputs, generalize well across unseen geometry-condition pairs.

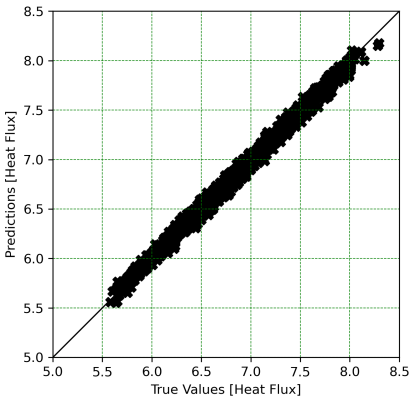

(a) Holdout – 2000 Points

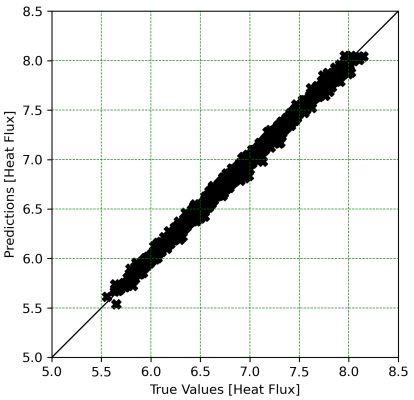

(b) Holdout – 2500 Points

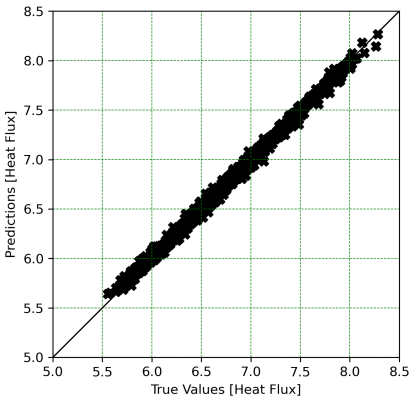

(c) Holdout – 3000 Points

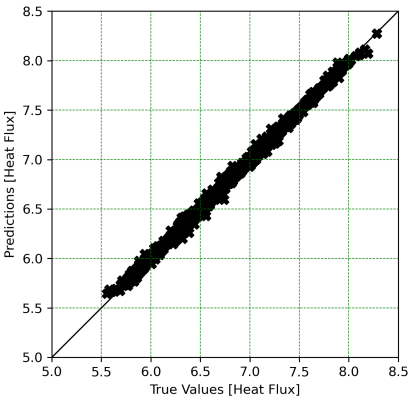

(d) Holdout – 3500 Points

Figure 9: Log10 True vs Predicted values for holdout data across different dataset sizes

DOI: 10.13009/EUCASS2025-722

Table 10: Hold set performance across dataset sizes

Design points	MAPE (%)	MAE	RMSE	R^2
2000	4.423	8.076e+05	3.079e+06	0.9736
2500	3.794	6.485e+05	2.575e+06	0.9812
3000	2.645	4.023e+05	1.821e+06	0.9905
3500	2.349	3.127e+05	1.543e+06	0.9927

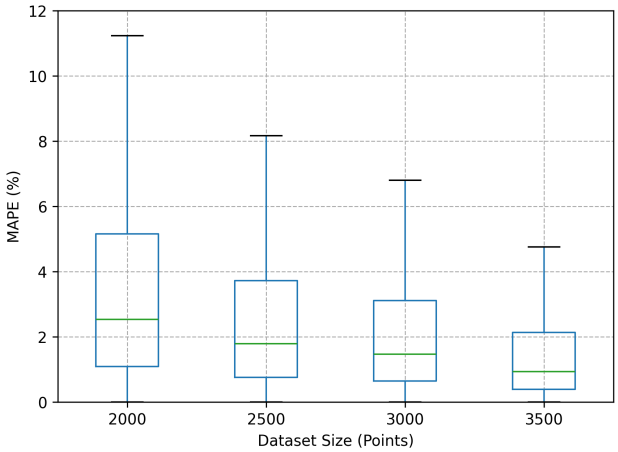

Figure 10: MAPE distribution across holdout splits

Figures 9 and 10 further support this observation, with scatter and error plots revealing tighter predictions and lower spread as training data increases. While some degradation in RMSE is inevitable in extrapolation, the R^2 values above 0.97 in all cases indicate that the model preserves the dominant data trends.

4. Conclusion

The proposed VAE-based surrogate modeling approach exhibits strong predictive performance for estimating stagnation point heat flux across a wide range of nose cone geometries and flight conditions. Using only 2000 training samples, which is approximately one-fourth of the full dataset, the model achieves a MAPE of 3.52 % on the test set and 4.42 % on the out-of-distribution test set, indicating accurate predictions even in sparse training regimes. This reduction from 8000 to 2000 simulations also lowers the total analysis time from 28 days to just 7 days. As the number of training points increases to 3500, the model achieves its best performance, reaching a test set MAPE of 1.99% and an out-of-distribution MAPE of 2.35 %. The R^2 values also remain consistently high across all configurations, even exceeding 0.99 in some extrapolative settings.

These results highlight the significance of combining latent representations from a variational autoencoder with a conditional MLP in addition to the robustness and scalability of the model. The ability to maintain strong accuracy under limited data while generalizing well to unseen geometry-condition pairs offers a compelling alternative to CFD simulations, significantly reducing computational costs.

Future work may extend this framework to full surface heat flux distributions and explore its applicability to more complex geometrical variations and flow conditions. Additionally, extrapolative performance and interpretability of the models could be improved by applying physics-based constraints or hybrid loss terms. Overall, the findings suggest an efficient path for tackling heat flux prediction challenges in hypersonic applications.

DOI: 10.13009/EUCASS2025-722

References

[1] Brandon Smith, Ethiraj Venkatapathy, Paul Wercinski, Bryan Yount, Dinesh Prabhu, Peter Gage, Lori Glaze, and Charles Baker. Venus in situ explorer mission design using a mechanically deployed aerodynamic decelerator. In *2013 IEEE Aerospace Conference*, pages 1–18. IEEE, 2013.

[2] Fred R DeJarnette, H Harris Hamilton, K James Weilmuenster, and F McNeil Cheatwood. A review of some approximate methods used in aerodynamic heating analyses. *Journal of Thermophysics and Heat Transfer*, 1(1):5–12, 1987.

[3] John David Anderson. *Hypersonic and high temperature gas dynamics*. Aiaa, 1989.

[4] M. Y. M. Ahmed and Ning Qin. Surrogate-based multi-objective aerothermodynamic design optimization of hypersonic spiked bodies. *28th International Symposium on Shock Waves*, pages 727–733, 2012.

[5] Dongming Ding, Hao Chen, Zheng Ma, Bin Zhang, and Hong Liu. Heat flux estimation of the cylinder in hypersonic rarefied flow based on neural network surrogate model. *AIP Advances*, 12(8):085314, 08 2022.

[6] Gang Dai, Wenwen Zhao, Shaobo Yao, and Weifang Chen. Machine learning strategy for wall heat flux prediction in aerodynamic heating. *Journal of Thermophysics and Heat Transfer*, 37(2):424–434, 2023.

[7] M. Raissi, P. Perdikaris, and G.E. Karniadakis. Physics-informed neural networks: A deep learning framework for solving forward and inverse problems involving nonlinear partial differential equations. *Journal of Computational Physics*, 378:686–707, 2019.

[8] Ameya D. Jagtap, Zhiping Mao, Nikolaus Adams, and George Em Karniadakis. Physics-informed neural networks for inverse problems in supersonic flows. *Journal of Computational Physics*, 466:111402, 2022.

[9] Myeong-Seok Go, Jae Hyuk Lim, and Seungchul Lee. Physics-informed neural network-based surrogate model for a virtual thermal sensor with real-time simulation. *International Journal of Heat and Mass Transfer*, 214:124392, 2023.

[10] Andres S. Padron, Juan J. Alonso, and Michael S. Eldred. Multi-fidelity methods in aerodynamic robust optimization. In *18th AIAA Non-Deterministic Approaches Conference*, 2016.

[11] Yunyang Zhang, Zhiqiang Gong, Weien Zhou, Xiaoyu Zhao, Xiaohu Zheng, and Wen Yao. Multi-fidelity surrogate modeling for temperature field prediction using deep convolution neural network. *Engineering Applications of Artificial Intelligence*, 123:106354, 2023.

[12] Hüseyin Avni Yaşar and Ercan Gürses. Adaptive-quadratic-neural-network-based multifidelity modeling approach for buckling of stiffened panels. *AIAA Journal*, 62(11):4207–4220, 2024.

[13] Huseyin Avni Yasar and Oguz Kaan Sevinc. Physics informed neural networks for enhanced critical heat flux prediction in hypersonic flows. In *AIAA AVIATION FORUM AND ASCEND 2024*, 2024.

[14] Saakaar Bhatnagar, Yaser Afshar, Shaowu Pan, Karthik Duraisamy, and Shailendra Kaushik. Prediction of aerodynamic flow fields using convolutional neural networks. *Computational Mechanics*, 64:525–545, 2019.

[15] Xu Wang, Weiqi Qian, Tun Zhao, Hai Chen, Lei He, Haisheng Sun, and Yuan Tian. A generative design method of airfoil based on conditional variational autoencoder. *Engineering Applications of Artificial Intelligence*, 139:109461, 2025.

[16] Kazuo Yonekura, Yuki Tomori, and Katsuyuki Suzuki. Airfoil shape generation and feature extraction using the conditional vae-wgan-gp. *AI*, 5(4):2092–2103, 2024.

[17] Kenneth E Tatum. Computation of thermally perfect properties of oblique shock waves. Technical report, 1996.

[18] Jianlong Yang and Meng Liu. A wall grid scale criterion for hypersonic aerodynamic heating calculation. *Acta Astronautica*, 136:137–143, 2017.

[19] H Julian Allen and Alfred J Eggers Jr. A study of the motion and aerodynamic heating of ballistic missiles entering the earth's atmosphere at high supersonic speeds. Technical report, 1958.

DOI: 10.13009/EUCASS2025-722

[20] Louis S Stiver. *Calculated Pressure Distributions and Components of Total-drag Coefficients for 18 Constant-volume Slender Bodies of Revolution at Zero Incidence for Mach Numbers from 2.0 to 12.0, with Experimental Aerodynamic Characteristics for Three of the Bodies*, volume 6536. National Aeronautics and Space Administration, 1971.

[21] Ashish Narayan, S Narayanan, and Rakesh Kumar. Hypersonic flow past nose cones of different geometries: a comparative study. *SIMULATION*, 94(8):665–680, 2018.

[22] Sheung Sher Chin. *Missile configuration design*. McGraw-Hill, 1961.

[23] Ronald L. Iman. Latin hypercube sampling. *John Wiley & Sons, Ltd*, 2008.

[24] Akhil Vakayil and V Roshan Joseph. Data twinning. *Statistical Analysis and Data Mining: The ASA Data Science Journal*, 15(5):598–610, 2022.

[25] Takuya Akiba, Shotaro Sano, Toshihiko Yanase, Takeru Ohta, and Masanori Koyama. Optuna: A next-generation hyperparameter optimization framework. In *Proceedings of the 25th ACM SIGKDD international conference on knowledge discovery & data mining*, pages 2623–2631, 2019.